Experimental and numerical investigations of crack growth of hot-rolled steel Q420C using cohesive zone model

DOI:
10.1016/j.tafmec.2023.104036

Document Version
Accepted author manuscript

Citation for published version (APA):
Chen, C.-J., Su, M.-N., Wang, Y.-H., & Zhu, R.-H. (2023). Experimental and numerical investigations of crack growth of hot-rolled steel Q420C using cohesive zone model. *Theoretical and Applied Fracture Mechanics*, *127*, Article 104036. https://doi.org/10.1016/j.tafmec.2023.104036

Published in:
Theoretical and Applied Fracture Mechanics

Chen, C.J., Su, M.N., Wang, Y.H., Zhu, R.H. (2023), "Experimental and numerical investigations of crack growth of hot-rolled steel Q420C using cohesive zone model", Theoretical and Applied Fracture Mechanics, 127:104036.

Experimental and numerical investigations of crack growth of hot-rolled steel Q420C using cohesive zone model

Chun-Jun Chen[a], Mei-Ni Su[b], Yu-Hang Wang[a,*], Rong-Hua Zhu[c]

a School of Civil Engineering, Chongqing University, Chongqing, China

b Department of Mechanical, Aerospace and Civil Engineering, The University of Manchester, Manchester, UK

c Yangjiang Offshore Wind Energy Laboratory, Guangdong 529533, China

Abstract: In this paper, the application problem of cyclic cohesive zone models at different load ratios is thoroughly studied based on test data of hot-rolled steel Q420C. Firstly, the fracture toughness of Q420C steel was measured and load-crack mouth opening displacement (F-CMOD) curves were recorded. Secondly, with the help of F-CMOD curves, a comparative study of monotonic cohesive zone models was performed to calibrate model parameters. Finally, cyclic cohesive zone models with different unloading-reloading paths were used to simulate the high-cycle fatigue crack growth behaviour of Q420C steel, and their performances were compared. Research results show that plane stress assumption is more sensible when the finite element model is simplified from 3D to 2D. Rather than the conditional fracture toughness K_Q, the elastic-plastic fracture toughness CTOD should be used to calculate the fracture energy of the monotonic cohesive zone model. Both cyclic cohesive zone models show good robustness towards the mesh size. When the linear scaling method is used to reduce simulation time, the cyclic cohesive zone model with an unloading-reloading path passing through the origin of coordinates is the better choice. To improve the simulation accuracy of cyclic cohesive zone models at different load ratios, the load ratio must be incorporated in the damage evolution law, and a linear relationship between accumulated cohesive length δ_Σ and load ratio R was proposed for engineering applications.

Keywords: cyclic cohesive zone model, fracture toughness, load ratio effect, linear scaling method, Q420C steel, simulation

1 Introduction

To capitalise on abundant wind energy, the erection of wind turbine towers is essential. When designing wind turbine towers, both the static and fatigue resistances must be taken into consideration. As for fatigue resistance, two design methods could be used. One is the stress-life (S-N) curve method, which ensures sufficient fatigue crack initiation life. The other is the fracture mechanics method, which is capable of predicting the remaining life of structures with long fatigue cracks [1].

To precisely estimate the remaining fatigue life of tower tubes, fatigue crack propagation tests are essential, although they are costly and time-consuming. With the progress of computer hardware and software, an alternative solution is to predict fatigue crack growth behaviour using numerical simulation. Up to now, great efforts have been devoted to coming up with fatigue crack growth simulation models. Among all of them, the extended finite element method (XFEM) [2–4] and the cyclic cohesive zone model (CCZM) [5–11] are the most widely used ones. XFEM modifies the element's shape function to consider discontinuity, particularly suitable for the analysis of static or dynamic crack growth; meanwhile, it does not require pre-defining crack paths, which facilitates the analysis of crack growth with changing directions. Nevertheless, XFEM may not be able to provide very precise remaining fatigue life in certain cases. By comparison, CCZM shows better performance in fatigue life estimation [12]. The CCZM includes three elements: the traction separation law, the unloading-reloading path, and the damage evolution law. Each element can be formulated in different ways. For example, the traction separation law can take triangular, trapezoidal, or exponential forms [9]. As for the unloading-reloading path, it could pass through the origin of coordinates or not. [13,14]. The damage evolution law has various expressions and its core task is to interpret the contribution of strain changes to damage accumulation during cycles. So far, a large number of CCZMs have been reported in the literature, but the effect of load ratio R on damage evolution law is still not clear. Li and Yuan [15] used a CCZM to simulate the fatigue crack growth behaviour of the nickel-based superalloy IN718 at different load ratios and proposed a linear equation relating accumulated cohesive length δ_{Σ} and the natural logarithm of load ratio R. Wei et al. [16] simulated the fatigue crack propagation of alloy steel $30CrNi_2MoV$ and found that good simulation results could be obtained with a constant value of accumulated cohesive length δ_{Σ}. Hu et al. [12] found that it was not necessary to include the load ratio R into the damage evolution law for the 304 austenitic stainless steel. As shown in the literature, no concensus has been reached for the effect of load ratios on the damage evolation law.

This paper will systematically study the effect of load ratios on CCZMs and propose a method to improve the accuracy of CCZMs. Firstly, the fracture toughness of Q420C steel is measured and F-CMOD curves are recorded. Secondly, based on F-CMOD curves, parameters (initial peak traction $\sigma_{max,0}$ and cohesive length δ_0) of the monotonic cohesive zone model are calibrated. Afterwards, a series of parametric studies of CCZMs are carried out to investigate the effects of important parameters including the mesh size, the linear scaling factor, the unloading-reloading path, and the load ratio. Finally, a correction factor regarding the load ratio is proposed to adjust the accumulated cohesive length δ_Σ to improve the accuracy of CCZMs at different load ratios.

2 Fracture toughness

2.1 Fracture toughness test

Three standard compact specimens, designated as DL1, DL2 and DL3, were used to test the fracture toughness of longitudinal cracks in the hot-rolled steel Q420C (Fig. 1a). Dimensions of the three specimens are congruent, which are shown in Fig. 1b. Fracture toughness tests were performed on a MTS 809 test system (Fig. 2) and included three steps. The first step was fatigue pre-crack, which offered a sharp crack in the specimen. Fatigue pre-crack adopted K-controlled loading with a load ratio of 0.1. The total length of fatigue pre-crack was 8 mm. In the initial phase of fatigue pre-crack, a relatively higher K_{max}(~ 35 MPa$\sqrt{\mathrm{m}}$) was chosen to accelerate crack initiation from the machined notch. In the last phase of fatigue pre-crack (about 3 mm), a relatively lower K_{max} (~ 20 MPa$\sqrt{\mathrm{m}}$) was employed to meet the requirements in GB/T 21143-2014 [17]. The loading frequency of fatigue pre-crack was 15 Hz. The crack length was monitored automatically by the MTS control station through a COD gauge.

The second step was monotonic loading to failure. After fatigue pre-crack, specimens were loaded under displacement control. During the loading process, the load F and the crack mouth opening displacement CMOD were recorded continuously. When the load F reached a peak and then tended to decrease, the loading was manually stopped.

The final step was the post-processing which included heat tinting and measurement of pre-fatigue crack lengths. The specific heat tinting process was as follows: all three specimens were heated to 500 °C, maintained for 30 minutes, and finally cooled naturally. After the heat tinting process, fracture surfaces already formed would appear darker, which facilitated the measurement of crack lengths. Subsequently, all three specimens were pulled apart by the MTS 809 test system. With an optical microscope, the nine-point average method [17] was used to determine the average crack length after fatigue pre-crack.

2.2 Fracture toughness calculation

First, the linear elastic conditional fracture toughness K_Q was calculated. In the F-CMOD graph, starting from the origin, a line was drawn with the slope being 5% less than the initial slope of the F-CMOD curve. This line intersected the F-CMOD curve at the point F_Q. Substitute F_Q into Equation (1) to calculate the condition value K_Q [17].

$$K_Q = \left[\frac{F_Q}{(BB_N W)^{0.5}}\right]\left[g_2\left(\frac{a_0}{W}\right)\right] \tag{1}$$

$$g_2\left(\frac{a_0}{W}\right) = \frac{\left(2+\frac{a_0}{W}\right)[0.886+4.64\frac{a_0}{W}-13.32\left(\frac{a_0}{W}\right)^2+14.72\left(\frac{a_0}{W}\right)^3-5.6(\frac{a_0}{W})^4]}{(1-\frac{a_0}{W})^{1.5}} \tag{2}$$

where F_Q is the conditional force corresponding to the small-scale yielding condition. B is the specimen thickness. B_N is the net thickness of the specimen when side grooves exist. W is the specimen width. $g_2(a/W)$ is the stress intensity factor coefficient. a_0 is the initial crack length, i.e. the fatigue pre-crack length.

Next, it was judged whether the conditional fracture toughness K_Q was equivalent to the plane strain fracture toughness K_{IC}. Find the peak on the F-CMOD curve and designate it as F_m. If the F_m/F_Q is larger than 1.1, the conditional fracture toughness K_Q is not equivalent to plane strain fracture toughness K_{IC}. The calculation results of the three specimens are summarised in Table 1. Obviously, the values of F_m/F_Q are all greater than 1.1. Therefore, the plane strain fracture toughness cannot be obtained and the elastic-plastic fracture toughness CTOD should be determined according to Equations (3)-(5) [17].

$$\delta = [\frac{F_m}{(BB_NW)^{0.5}} \times g_2(\frac{a_0}{W})]^2 \left[\frac{(1-\nu^2)}{2R_{p0.2}E}\right] + \frac{(RO-a_0-Z)V_p}{RO} \tag{3}$$

$$R = \frac{(a_0/W)^2}{1-a_0/W} Wg(a_0/W) \tag{4}$$

$$g(a_0/W) = 150.1554 - 1427.620(a_0/W) + 5712.630(a_0/W)^2 - 12131.870(a_0/W)^3 + 14357.50(a_0/W)^4 - 8967.939(a_0/W)^5 + 2309.530(a_0/W)^6 \tag{5}$$

where ν is the Poisson ratio. E is Young's modulus. $R_{P0.2}$ is the yield strength. RO is the rotational radius. Z is the distance between the mounting position of the extensometer and the surface of the specimen. V_p is the plastic component in the opening displacement of the extensometer.

Since the value of elastic-plastic fracture toughness CTOD is size-sensitive, the specimen thickness should be indicated in the footnote to the toughness symbol. In addition, the load type used in the calculation should also be reflected in the toughness symbol. In this paper, the maximum load was used, hence the letter m needed to be included in the footnote. Considering these two points, the symbol for fracture toughness CTOD was $\delta_{m(12)}$.

3 Cyclic cohesive zone model

The cyclic cohesive zone model consists of three elements, namely the traction separation law, the damage evolution law, and the unloading-reloading path. Specific expressions for these three elements are discussed in detail in the following sections.

3.1 Traction separation law

The traction separation law proposed by Roe and Siegmund [13] is in an exponential form. The normal traction and shear traction could be determined as follows [13]:

$$T_n = \sigma_{max,0} e exp\left(-\frac{\Delta u_n}{\delta_0}\right)\left\{\frac{\Delta u_n}{\delta_0}\exp\left(-\frac{\Delta u_t^2}{\delta_0^2}\right) + (1.0-q)\frac{\Delta u_n}{\delta_0}\left[1.0-\exp\left(-\frac{\Delta u_t^2}{\delta_0^2}\right)\right]\right\} \quad (6)$$

$$T_t = 2\sigma_{max,0} e q \frac{\Delta u_t}{\delta_0}\left(1.0+\frac{\Delta u_n}{\delta_0}\right) exp\left(-\frac{\Delta u_n}{\delta_0}\right) exp\left(-\frac{\Delta u_t^2}{\delta_0^2}\right) \quad (7)$$

where $\sigma_{max,0}$ is the initial normal cohesive strength, i.e. the maximum normal traction reached during monotonic loading to failure. Δu_n and Δu_t are normal and shear separation, respectively. δ_0 is the cohesive length, i.e., the separation corresponding to $\sigma_{max,0}$. Parameter q is the ratio between shear cohesive surface energy $\varphi_{t,0} = \sqrt{e/2}\,\tau_{max,0}\delta_0$ and normal cohesive surface energy $\varphi_{n,0} = \sigma_{max,0}\delta_0 e$. $\tau_{max,0}$ is the initial shear cohesive strength.

For the pure type I crack propagation, the shear traction on the crack path is always equal to zero. Therefore, Equations (6) and (7) could be simplified as follows:

$$T_n = \sigma_{max,0}\frac{\Delta u_n}{\delta_0} exp\left(1.0-\frac{\Delta u_n}{\delta_0}\right) \quad (8)$$

$$T_t = 0 \quad (9)$$

In the case of monotonic loading, the traction could be determined completely with Equations (8) and (9). For cyclic loading, the initial normal cohesive strength $\sigma_{max,0}$ needs to be replaced with the current cohesive strength σ_{max} using equation $\sigma_{max} = \sigma_{max,0}(1-D)$. Parameter D indicates the accumulated damage in cohesive elements, which ranges from 0 to 1.

3.2 Damage evolution law

During cyclic loading, the damage in cohesive elements accumulates gradually and reaches the critical value eventually. The accumulated damage can be determined by a damage evolution equation. For example, Roe and Siegmund proposed Equation (10) to calculate damage [13].

$$\dot{D} = \frac{|\Delta \dot{u}_n|}{\delta_\Sigma}\left\langle\frac{T_n}{\sigma_{max}} - C_f\right\rangle H(\overline{\Delta u_n} - \delta_0) \quad (10)$$

where δ_Σ is the accumulated cohesive length used to normalise the separation increment. C_f is the endurance limit ratio determined by the equation $C_f = \sigma_f/\sigma_{max,0}$. σ_f is the endurance limit. $\overline{\Delta u_n}$ is the accumulated material separation calculated by $\overline{\Delta u_n} = \int |\Delta \dot{u}_n|\, dt$. Macaulay brackets $\langle\,\rangle$ indicates that damage can only occur when the normal traction is greater than a certain positive value. Heaviside function $H()$ suggests that the damage starts to evolve as the accumulated separation increment reaches the cohesive length δ_0.

3.3 Unloading-reloading path

There are two types of unloading-reloading paths. The first path is analogous to the elastic-plastic behaviour. A residual separation exists when the normal traction is completely unloaded. The normal traction of the first path can be calculated according to Equation (11) [13,18].

$$T_n = T_{n,max} + k_n(\Delta u_n - \Delta u_{n,max}) \quad (11)$$

where $\Delta u_{n,max}$ is the maximum normal separation reached during the whole loading history. $T_{n,max}$ is the normal traction corresponding to $\Delta u_{n,max}$. k_n is equal to $\sigma_{max} e/\delta_0$.

The second path is analogous to the purely elastic behaviour. Specifically, the traction separation curve could pass through the origin of coordinates. The normal traction of the second path can be calculated using Equation (12) [19].

$$T_n = T_{n,max} + \frac{T_{n,max}}{\Delta u_{n,max}} (\Delta u_n - \Delta u_{n,max}) \tag{12}$$

3.4 Acceleration strategy

High-cycle fatigue tests usually take a long time. The cycle number reached before the final failure could be up to millions. Therefore, the cycle-by-cycle simulation strategy is impractical. To accomplish high-cycle fatigue crack growth simulation, three acceleration simulation methods have been proposed, i.e. the linear scaling method [12,16,20,21], the linear extrapolation method [22–30], and the envelope method [31–33]. The linear scaling method introduces a linear scaling factor β into the damage evolution law. In this way, the material can reach failure in a relatively small number of cycles. In the post-process, multiply simulated cycle numbers by β to obtain the predicted cycle number. The linear extrapolation method incorporates the features of both the cycle-by-cycle method and the linear scaling method. Specifically, it firstly simulates three or five cycles by the cycle-by-cycle method. Afterwards, it calculates every cycle's damage contribution. Finally, it multiplies the average damage increment by the number of several cycles as the damage contribution of next few simulation cycles. By repeating these three steps, the simulation time of high-cycle fatigue tests can be significantly reduced. The envelope method replaces the cyclic loading with static loading and correlates the damage increment with the loading time. In summary, each of the three acceleration methods has its own advantages. In this paper, only the linear scaling method was employed, because it is easy to program.

4 Monotonic loading simulation

4.1 Development of finite element models

The fracture toughness test was simulated using the Abaqus software [34]. To reduce the number of elements, the 3D specimen was simplified into a 2D model. Considering the symmetry of the specimen, only one-half of the whole model was established to further reduce the model size. The established model comprises a parent region and a cohesive element region. During loading, the stiffness of cohesive elements degrades gradually when element damage starts to accumulate. The stiffness degradation usually causes convergence issues. The Abaqus help documentation recommends utilising a viscosity coefficient to facilitate convergence. Through trial and error, it is found that augmenting the viscosity coefficient can significantly improve convergence. Nevertheless, the increased viscosity coefficient will also affect simulation results and influence further analysis. An alternative solution to convergence issues is to adopt fine meshes in the cohesive element region. Although this solution eliminates the need to introduce viscosity coefficients, it requires more elements and consumes more computational time. To limit the computational time, transitional meshes were used in the parent region. The generated transitional meshes are presented in Fig. 4, containing 7 transitional layers. Uniform meshes were used in the cohesive element region. The cohesive elements measure 0.01 mm in length and 0 mm in thickness. Cohesive elements share boundaries with the bottom elements of the parent region.

The cohesive element type was the 2D 4-node cohesive element COH2D4. Literature [16,20,35–37] suggests that the plane strain assumption should be used when specimen thickness is in the range of 9-12.5 mm. Literature [12,38] argues that when the CT specimen thickness is in the range of 3-5 mm, the plane stress assumption should be used. The authors of this paper believe that a thickness of 12 mm may not allow most of the crack front to reach the plane strain state. Given this, elements of the parent region were set to 4-node plane strain element CPE4 and 4-node plane stress element CPS4, respectively. Both simulation results will be compared to find out the proper stress state assumption. The Young's modulus of the parent region was set to 2.06×10^5 MPa and the Poisson's ratio was set to 0.3. The plastic behaviour of the parent region complied with the law of kinematic hardening, and the plastic parameters were set according to the true stress-strain curve of Q420C steel. The material behaviour of cohesive elements was set by a UMAT subroutine, which was programmed based on the monotonic cohesive zone model. The monotonic cohesive zone model is equivalent to the cyclic cohesive zone model that only includes the traction separation law. Literature [39] recommends that the initial normal cohesive strength $\sigma_{max,0}$ for the plane strain state takes $3\sigma_y$~$4\sigma_y$, and the $\sigma_{max,0}$ for the plane stress state takes $2\sigma_y$. In this paper, $\sigma_{max,0}$ was set to $2\sigma_y$, $2.5\sigma_y$, and $3\sigma_y$ for both the plane strain assumption and the plane stress assumption. The cohesive length δ_0 is determined from the total energy Γ of the monotonic cohesive zone model with the equation $\Gamma = \sigma_{max,0}\delta_0 e$. In theory, the total energy Γ is equal to the energy release rate G. Under the condition of small-scale yielding, for the plane strain condition, $G_I = (1-\nu^2)/E \cdot K_I^2$, $G_I = CTOD \cdot \pi \cdot \sigma_y/[4 \cdot (1-2\nu)]$; for the plane stress condition, $G_I = 1/E \times K_I^2$, $G_I = CTOD \cdot \pi \cdot \sigma_y/4$. The fracture toughness parameters K_Q and $\delta_{m(12)}$ were substituted into these equations, respectively, and the corresponding δ_0 was calculated. Parameters used in all simulation cases are summarised in Table 2.

4.2 Results and discussions

The contrast between the simulation and experimental results is presented in Fig. 5. The first number in the legend represents the initial normal cohesive strength $\sigma_{max,0}$ and the second number represents the cohesive length δ_0. The element type of the parent region is placed in parentheses. For plane strain cases where parameters are calculated by $\delta_{m(12)}$, as $\sigma_{max,0}$ increases, the maximum load that can be achieved also rises, and a load plateau tends to appear. With the decrease of $\sigma_{max,0}$, the maximum load obtained in simulation may be equal to the test results, but the F-CMOD curve will drop rapidly after the maximum load. For plane strain cases where parameters are calculated by K_Q, the maximum load achieved in simulation is much smaller than the test values. In addition, the bearing capacity of the specimen decreases rapidly after the peak load. The reason is that when cohesive elements fail, the absorbed energy is too small. Therefore, it can be concluded that the plane strain assumption is not suitable for the monotonic loading simulation of the 12 mm thick CT specimen.

For six plane stress cases (Fig. 5b), except the case where $\sigma_{max,0}$=860 MPa and δ_0=0.00661 mm, the F-CMOD curves of other cases are all close to experimental values. Quantitatively analysing the maximum load and corresponding CMOD, analysis results are summarised in Table 3. The comparison shows that the case where $\sigma_{max,0}$=860 MPa and δ_0=0.03092 mm is the closest to the experimental values. Thus, a conclusion can be drawn that the plane stress assumption is more suitable for the monotonic loading simulation of the 12 mm thick CT specimen. When the conditional fracture toughness K_Q is not equal to the plane strain fracture toughness K_{IC}, the elastic-plastic fracture toughness CTOD should be used to calculate the δ_0.

5 Cyclic loading simulation

5.1 FEM model configuration

In contrast to the monotonic loading simulation, the computational cost of the cyclic loading simulation dramatically increases with the increasing cycles. To reduce the computational cost of high-cycle fatigue simulation, a new meshing strategy is adopted in this section, which increases the size of bottom elements in the parent region, changes the connection method between parent region elements and cohesive elements from shared edges to bound boundaries, and makes the cohesive element size smaller than the size of bottom elements in the parent region. The resulting mesh is shown in Fig. 6. The minimum parent region element size is 0.1 mm, and three layers of transitional meshes are used to link the coarse and fine mesh areas. Cohesive elements measure 0 mm in thickness and 0.02 mm in length.

Based on the conclusions in Section 4, element type CPS4 was employed in the parent region and element type COH2D4 was chosen in the cohesive element region. The material behaviour in the parent region complies with the law of kinematic hardening. The elastoplastic parameters are set according to the true stress-strain curve of Q420C steel. Cohesive elements adopt two different CCZMs. The first CCZM employs the first unloading-reloading path and is designated as v25. The second CCZM adopts the second unloading-reloading path and is designated as v35. The loading waveform, the maximum load, and the load ratio used in the simulation are all consistent with the practical test parameters. Endurance limit ratio C_f is set as 0.25. Accumulated cohesive length δ_Σ equals $\alpha\delta_0$. Parameter α adjusts the rate of damage accumulation according to the load ratio, and improves the accuracy of simulation results. α is related to both the material property and the load ratio. The linear scaling method is used to reduce simulation time, and the effect of the linear scaling factor β is studied by setting β/α to 0.125, 0.25, 0.5, 1, and 2. Finally, the robustness of CCZMs is examined by changing the cohesive element size (from 0.02 mm to 0.04 mm and 0.08 mm), and changing the bottom parent region element size (from 0.1 mm to 0.2 mm and 0.4 mm).

5.2 The effect of load ratio and linear scaling factor

In the post-processing module of ABAQUS, a Python script is created to automatically obtain the crack length a – cycle number N curve from simulation results. The $a-N$ curve at $\beta/\alpha=0.25$ is used as a benchmark, and the most appropriate value of linear scaling factor β is found by trial calculations with an increment of 50. For cases where β/α takes other values, the value of β is scaled up or down. In the post-process, the number of simulated cycles is multiplied by the corresponding β, and the processed results are presented in Fig. 7(a-b) and Fig. 8(a-b). Only $a-N$ curves at $\beta/\alpha=0.125$ or 0.25 are further processed by the 7-points incremental polynomial method [40] to obtain rate curves, and the obtained rate curves are shown in Fig. 7(c-d) and Fig. 8(c-d). The experimental data in Fig. 7 and Fig. 8 are extracted from the literature [41]. In the legend, v25 and v35 are the model numbers, respectively. R01 and R03 represent load ratios. The number following the letter x represents β/α. The number in parentheses stands for β.

For the cyclic cohesive zone model v25, a larger β/α could shorten simulation time, but also reduce the propagation distance. It can be seen from $a-N$ curves that, as β/α increases, the crack growth rate at a given ΔK in the later stages increases. Therefore, to obtain accurate simulation results, the value of β/α should not be too large. As β/α decreases, the difference between simulated $a-N$ curves gradually decreases. Nevertheless, the value of β/α cannot be too small, because too small a value of β/α would considerably increase computational time and cause an abnormal drop in crack growth rates in the later stages. By trial and error calculation, it is found that β/α=0.25 is the most suitable value when using the CCZM v25. In addition, the load ratio affects the value of β. When β/α is equal to 0.25, β can take the value of 250 at a load ratio of 0.1, and take the value of 400 at a load ratio of 0.3.

The results simulated with CCZM v35 differ significantly from those with CCZM v25 in several respects. Firstly, a larger β/α would lead to a smaller rate at the same ΔK in the later stages. Secondly, when β/α takes a small value, there is no abnormal drop in the rate curves. Thirdly, as β/α decreases, the difference between simulated $a-N$ curves decreases quickly. It can be seen from Fig. 8(a-b) that when β/α equals 0.125 or 0.25, the $a-N$ curves are identical. Finally, When β/α is equivalent to 0.25, in cases of CCZM v35, β can take the value of 350 at a load ratio of 0.1, and take the value of 600 at a load ratio of 0.3.

Considering that the test involves only two load ratios (0.1 and 0.3), a linear relationship $\alpha = kR + b$ is herein suggested to reflect the effect of the load ratio on parameter α. By fitting analysis, the specific expression of this linear relationship in both CCZMs is as follows:

For CCZM v25: $$\alpha = 3000R + 700 \tag{13}$$

For CCZM v35: $$\alpha = 5000R + 900 \tag{14}$$

5.3 The robustness study

For robustness studies, the simulation results of CCZMs are shown in Fig. 9. In the legend, v25 and v35 represent the model numbers of CCZMs. R01 and R03 are load ratios. The number following the letter x stands for β/α. The first number in parentheses is the minimum element size in the parent region, and the second number represents the length of cohesive elements. The purpose of robustness studies is to examine the influence of different mesh sizes on simulation results, so β/α is set as a constant value of 0.25. It can be seen from the simulation results that under the same loading condition, the variation of mesh size does not affect simulation results. Therefore, a conclusion can be drawn that CCZMs have good robustness when simulating the high-cycle fatigue crack growth behaviour of Q420C steel.

5.4 Application suggestions

In conjunction with the findings of the previous subsections, a few suggestions can be made for the application of CCZMs to the high-cycle fatigue crack propagation simulation. For the two CCZMs with different unloading-reloading paths, the second path should be preferred in applications. When meshing is performed, the coarse mesh is first used for the trial calculation, and the mesh is then gradually refined until fatigue cracks propagate successfully without convergence issues. In the damage evolution law, β/α could be set to 0.25. In the post-process, parameter β is determined by fitting experimental data or calculated through α from Equations (13) or (14).

6 Conclusions

In this study, fracture toughness tests were carried out on hot-rolled steel Q420C. The parameters of the monotonic cohesive zone model are calibrated based on the toughness test data. Finally, the simulation accuracy and robustness of the two cyclic cohesive zone models are investigated. Research results show that longitudinal cracks in the Q420C steel sheet exhibit ductile fracture in toughness tests. As Q420C steel has excellent toughness, the elastic-plastic fracture toughness CTOD should be used to calculate the fracture energy of the monotonic cohesive zone model, rather than the conditional fracture toughness K_Q. When simplifying 3D 12 mm thick specimens to 2D models, the plane stress assumption is more appropriate than the plane strain assumption. Cyclic cohesive zone models have good robustness to mesh sizes, no matter which unloading-reloading path is adopted. Furthermore, the cyclic cohesive zone model whose unloading-reloading path through the origin of coordinates is the better choice for engineering applications.

Acknowledgement

The authors would like to acknowledge the support of the National Natural Science Foundation of China 52278144 and Fundamental Research Funds for the Central Universities 2022CDJQY-009.

References

[1] Schijve J. Fatigue of structures and materials. Second edition. Dordrecht: Springer; 2009.

[2] Xin H, Correia JAFO, Veljkovic M. Three-dimensional fatigue crack propagation simulation using extended finite element methods for steel grades S355 and S690 considering mean stress effects. Eng Struct 2021;227:111414. https://doi.org/10.1016/j.engstruct.2020.111414.

[3] Zhao Q, Abdel Wahab M, Ling Y, Liu Z. Fatigue crack propagation across grain boundary of Al-Cu-Mg bicrystal based on crystal plasticity XFEM and cohesive zone model. Journal of Materials Science & Technology 2022;126:275–87. https://doi.org/10.1016/j.jmst.2022.03.020.

[4] Zhao Q, Abdel Wahab M, Ling Y, Liu Z. Fatigue crack propagation within Al-Cu-Mg single crystals based on crystal plasticity and XFEM combined with cohesive zone model. Materials & Design 2021;210:110015. https://doi.org/10.1016/j.matdes.2021.110015.

[5] Tserpes K, Barroso-Caro A, Carraro PA, Beber VC, Floros I, Gamon W, et al. A review on failure theories and simulation models for adhesive joints. The Journal of Adhesion 2021;0:1–61. https://doi.org/10.1080/00218464.2021.1941903.

[6] Yuan H, Li X. Critical remarks to cohesive zone modeling for three-dimensional elastoplastic fatigue crack propagation. Engineering Fracture Mechanics 2018;202:311–31. https://doi.org/10.1016/j.engfracmech.2018.03.018.

[7] Jimenez S, Duddu R. On the parametric sensitivity of cohesive zone models for high-cycle fatigue delamination of composites. International Journal of Solids and Structures 2016;82:111–24. https://doi.org/10.1016/j.ijsolstr.2015.10.015.

[8] Kuna M, Roth S. General remarks on cyclic cohesive zone models. Int J Fract 2015;196:147–67. https://doi.org/10.1007/s10704-015-0053-y.

[9] Park K, Paulino GH. Cohesive Zone Models: A Critical Review of Traction-Separation Relationships Across Fracture Surfaces. Applied Mechanics Reviews 2013;64. https://doi.org/10.1115/1.4023110.

[10] Liu J, Li J, Wu B. The Cohesive Zone Model for Fatigue Crack Growth. Advances in Mechanical Engineering 2013;5:737392. https://doi.org/10.1155/2013/737392.

[11] Nguyen KD, Thanh C-L, Vogel F, Nguyen-Xuan H, Abdel-Wahab M. Crack propagation in quasi-brittle materials by fourth-order phase-field cohesive zone model. Theoretical and Applied Fracture Mechanics 2022;118:103236. https://doi.org/10.1016/j.tafmec.2021.103236.

[12] Hu X, Xu J, Du X, Zhang Y, Zhou F. Research on Fatigue Crack Propagation of 304 Austenitic Stainless Steel Based on XFEM and CZM. Metals 2020;10:727. https://doi.org/10.3390/met10060727.

[13] Roe KL, Siegmund T. An irreversible cohesive zone model for interface fatigue crack growth simulation. Engineering Fracture Mechanics 2003;70:209–32. https://doi.org/10.1016/S0013-7944(02)00034-6.

[14] Wang B, Siegmund T. A numerical analysis of constraint effects in fatigue crack growth by use of an irreversible cohesive zone model. Int J Fract 2005;132:175–96. https://doi.org/10.1007/s10704-005-0627-1.

[15] Li H, Yuan H. Cohesive zone modelling of low cycle fatigue cracks in cracked and notched specimens. Fatigue & Fracture of Engineering Materials & Structures 2013;36:1246–57. https://doi.org/10.1111/ffe.12061.

[16] Wei C, Zhou S, Li M, Zhang S. Numerical investigation on fatigue crack growth of fracturing pump head using cohesive zone model. Theoretical and Applied Fracture Mechanics 2020;107:102564. https://doi.org/10.1016/j.tafmec.2020.102564.

[17] GB/T 21143-2014. Metallic materials - Unified method of test for determination of quasistatic fracture toughness. 2014.

[18] Siegmund T. A numerical study of transient fatigue crack growth by use of an irreversible cohesive zone model. International Journal of Fatigue 2004;26:929–39. https://doi.org/10.1016/j.ijfatigue.2004.02.002.

[19] Wang B, Siegmund T. Numerical simulation of constraint effects in fatigue crack growth. International Journal of Fatigue 2005;27:1328–34. https://doi.org/10.1016/j.ijfatigue.2005.06.001.

[20] Ural A, Krishnan VR, Papoulia KD. A cohesive zone model for fatigue crack growth allowing for crack retardation. International Journal of Solids and Structures 2009;46:2453–62. https://doi.org/10.1016/j.ijsolstr.2009.01.031.

[21] Zhang W, Tabiei A. Improvement of an Exponential Cohesive Zone Model for Fatigue Analysis. J Fail Anal and Preven 2018;18:607–18. https://doi.org/10.1007/s11668-018-0434-4.

[22] Bouvard JL, Chaboche JL, Feyel F, Gallerneau F. A cohesive zone model for fatigue and creep–fatigue crack growth in single crystal superalloys. International Journal of Fatigue 2009;31:868–79. https://doi.org/10.1016/j.ijfatigue.2008.11.002.

[23] Jiang H, Gao X, Srivatsan TS. Predicting the influence of overload and loading mode on fatigue crack growth: A numerical approach using irreversible cohesive elements. Finite Elements in Analysis and Design 2009;45:675–85. https://doi.org/10.1016/j.finel.2009.05.006.

[24] Ghovanlou MK, Jahed H, Khajepour A. Cohesive zone modeling of fatigue crack growth in brazed joints. Engineering Fracture Mechanics 2014;120:43–59. https://doi.org/10.1016/j.engfracmech.2014.03.014.

[25] Nojavan S, Schesser D, Yang QD. A two-dimensional in situ fatigue cohesive zone model for crack propagation in composites under cyclic loading. International Journal of Fatigue 2016;82:449–61. https://doi.org/10.1016/j.ijfatigue.2015.08.029.

[26] Nojavan S, Schesser D, Yang QD. An in situ fatigue-CZM for unified crack initiation and propagation in composites under cyclic loading. Composite Structures 2016;146:34–49. https://doi.org/10.1016/j.compstruct.2016.02.060.

[27] Nijin IS, Shravan Kumar R, Banerjee A. Role of stress-state on initiation and growth of a fatigue crack. International Journal of Fatigue 2019;118:298–306. https://doi.org/10.1016/j.ijfatigue.2018.02.031.

[28] Salih S, Davey K, Zou Z. A computationally efficient cohesive zone model for fatigue. Fatigue & Fracture of Engineering Materials & Structures 2019;42:518–32. https://doi.org/10.1111/ffe.12927.

[29] Ibrahim GR, Albarbar A, Brethee KF. Progressive failure mechanism of laminated composites under fatigue loading. J Compos Mater 2021;55:137–44. https://doi.org/10.1177/0021998320944990.

[30] Nijin IS, Banerjee A. An incremental elastic–plastic triaxiality dependent fatigue model. Int J Fract 2021;227:39–55. https://doi.org/10.1007/s10704-020-00494-8.

[31] Jimenez S, Liu X, Duddu R, Waisman H. A discrete damage zone model for mixed-mode delamination of composites under high-cycle fatigue. Int J Fract 2014;190:53–74. https://doi.org/10.1007/s10704-014-9974-0.

[32] Eva S. Development of a Fatigue Analysis Tool Using Cohesive Zone Modelling for Composite Specimens. Master. Delft University of Technology, 2019.

[33] Tserpes K, Floros I. Fatigue crack growth simulation in adhesively bonded composite joints. Fatigue & Fracture of Engineering Materials & Structures 2019;42:1430–40. https://doi.org/10.1111/ffe.12969.

[34] SIMULIA User Assistance 2020.

[35] Li H, Yuan H, Li X. Assessment of low cycle fatigue crack growth under mixed-mode loading conditions by using a cohesive zone model. International Journal of Fatigue 2015;75:39–50. https://doi.org/10.1016/j.ijfatigue.2015.01.008.

[36] Yuan H, Li H, Li X. Prediction of Low Cycle Fatigue Crack Growth under Mixed-mode Loading Conditions Using Cohesive Zone Models. Procedia Engineering 2015;99:1317–22. https://doi.org/10.1016/j.proeng.2014.12.665.

[37] Li H, Li J, Yuan H. Application of a Cohesive Zone Model for Simulating Fatigue Crack Growth from Moderate to High Levels of Inconel 718. International Journal of Aerospace Engineering 2018;2018:e4048386. https://doi.org/10.1155/2018/4048386.

[38] Silitonga S, Maljaars J, Soetens F, Snijder HH. Numerical Simulation of Fatigue Crack Growth Rate and Crack Retardation due to an Overload Using a Cohesive Zone Model. Advanced Materials Research 2014;891–892:777–83. https://doi.org/10.4028/www.scientific.net/AMR.891-892.777.

[39] Liu J, Xiang C, Yuan H. Prediction of 3D small fatigue crack propagation in shot-peened specimens. Computational Materials Science 2009;46:566–71. https://doi.org/10.1016/j.commatsci.2009.03.011.

[40] Chen C-J, Su M-N, Wang Y-H, Deng X-W. Experimental research on the fatigue crack growth behaviour of Q420C. Journal of Constructional Steel Research 2022;192:107241. https://doi.org/10.1016/j.jcsr.2022.107241.

[41] Chen C-J, Su M-N, Wang Y-H, Zhu R-H. Experimental investigation on anisotropic fatigue crack growth characteristics of Q420C steel. Theoretical and Applied Fracture Mechanics

2023:103815. https://doi.org/10.1016/j.tafmec.2023.103815.

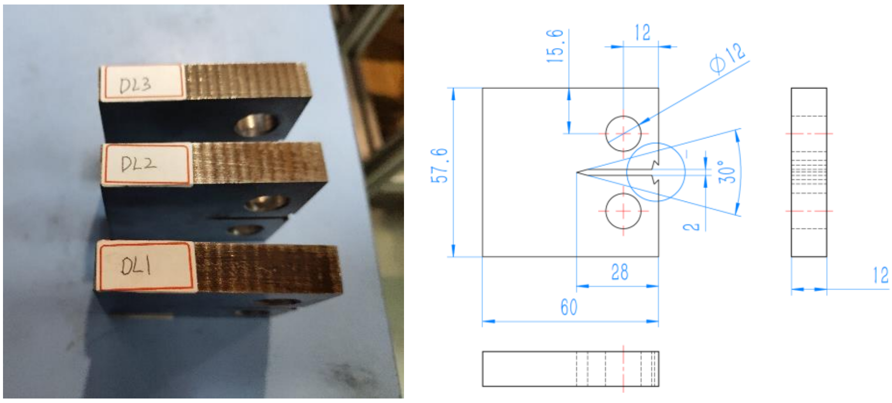

(a) (b)

Fig. 1. Specimens (a) labels, (b) dimensions (unit: mm).

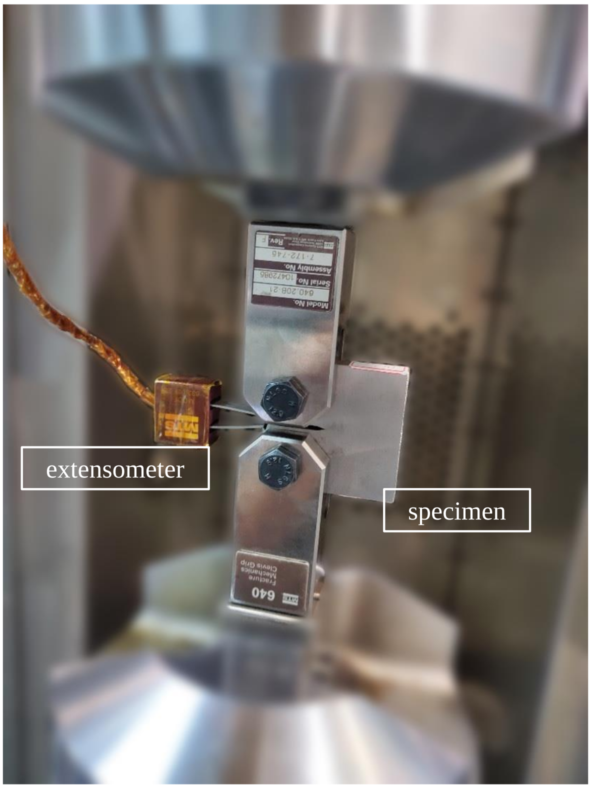

Fig. 2. Fracture toughness test.

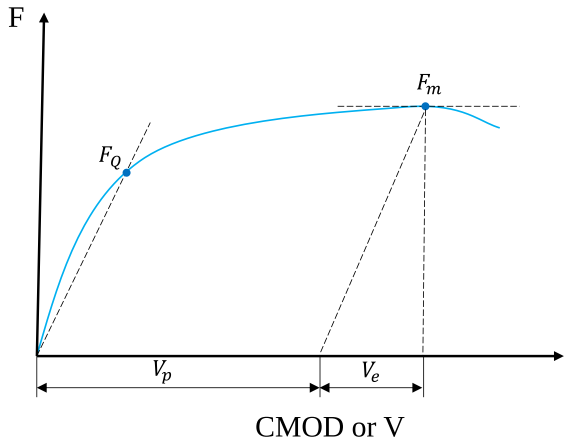

Fig. 3. Typical forces of fracture toughness determination in the F-CMOD curve.

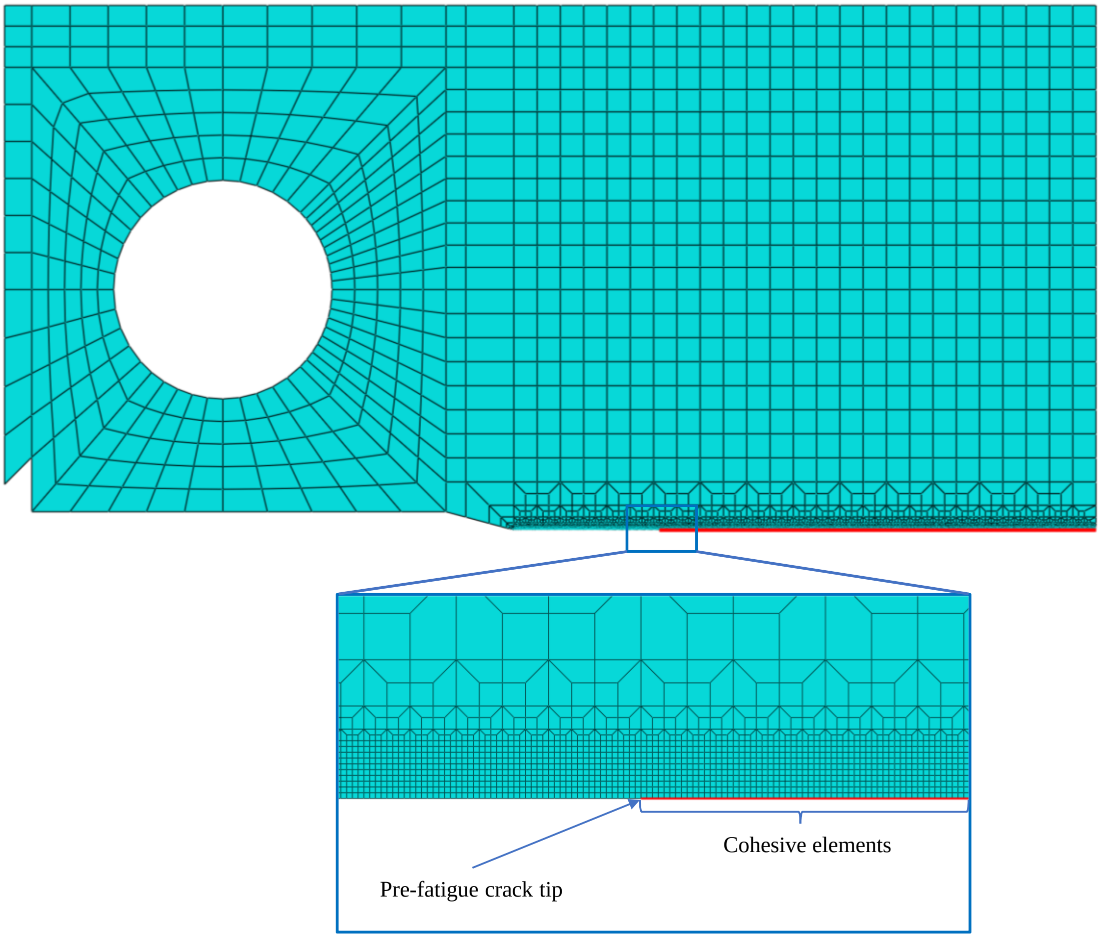

Fig. 4. Transitional mesh configuration of the CT specimen (half model for the monotonic loading simulation).

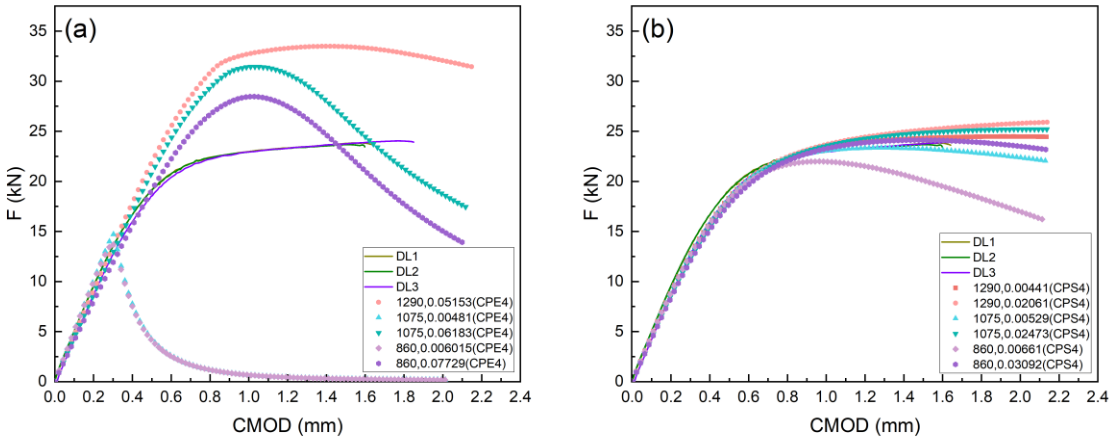

Fig. 5. Simulation results of fracture toughness tests. (a) plane strain case, (b) plane stress case.

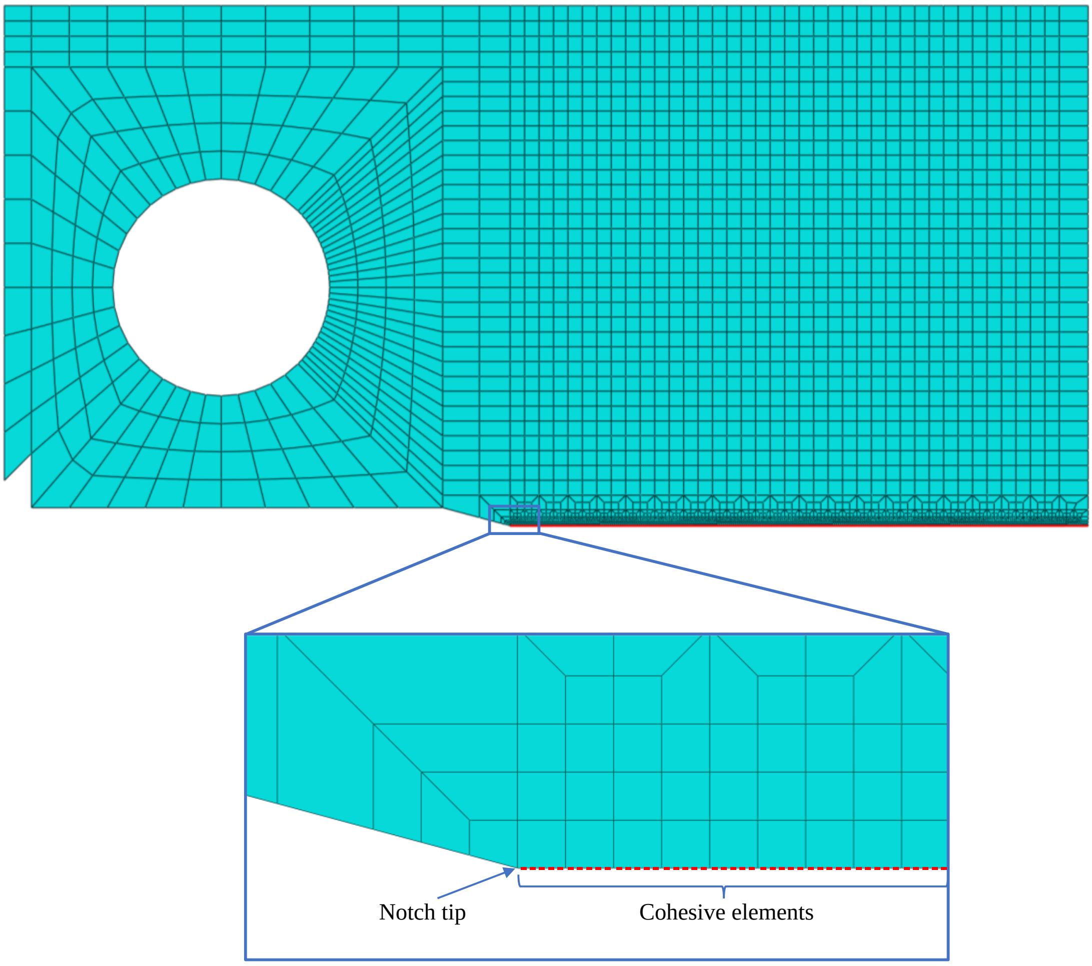

Fig. 6. Transitional mesh configuration of the CT specimen (half model for the cyclic loading simulation).

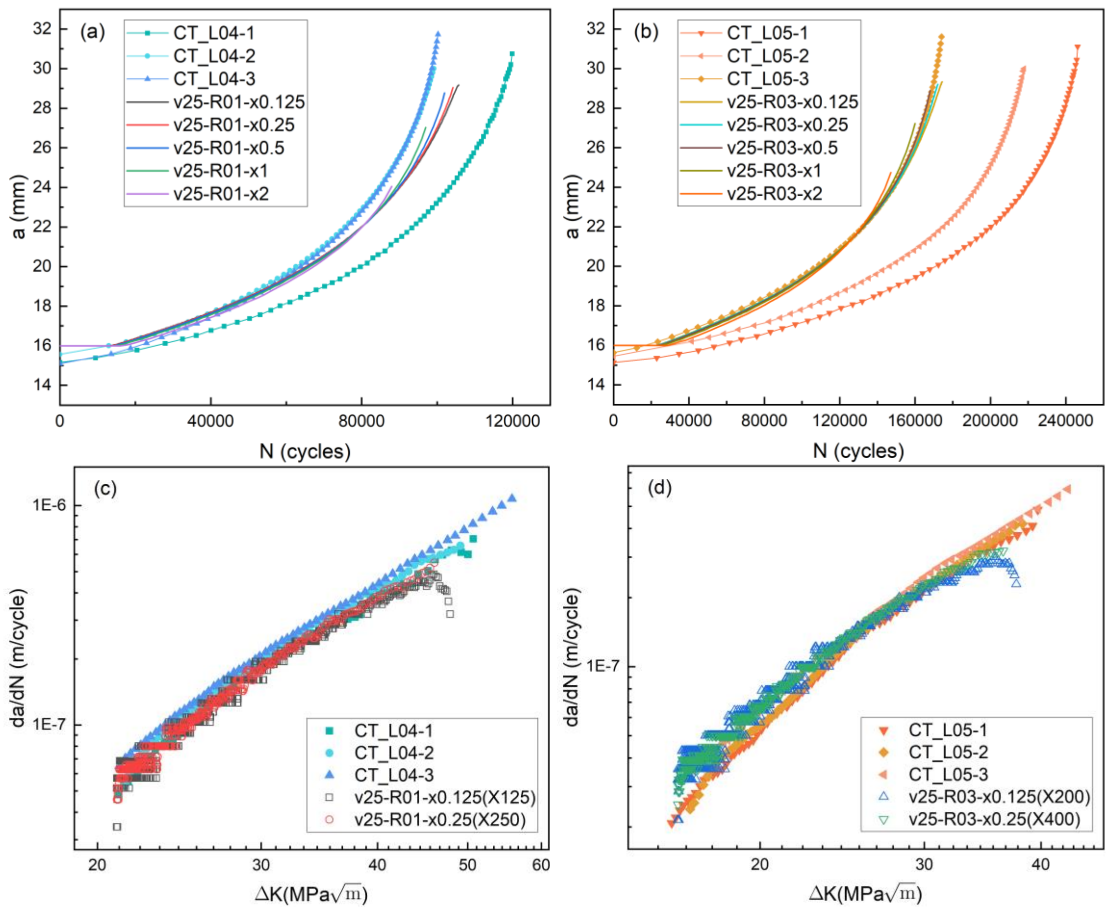

Fig. 7. Simulation results of CCZM v25. (a) $a - N$ curves at the load ratio of 0.1, (b) $a - N$ curves at the load ratio of 0.3, (c) rate curves at the load ratio of 0.1, and (d) rate curves at the load ratio of 0.3. (test data are extracted from Ref [41])

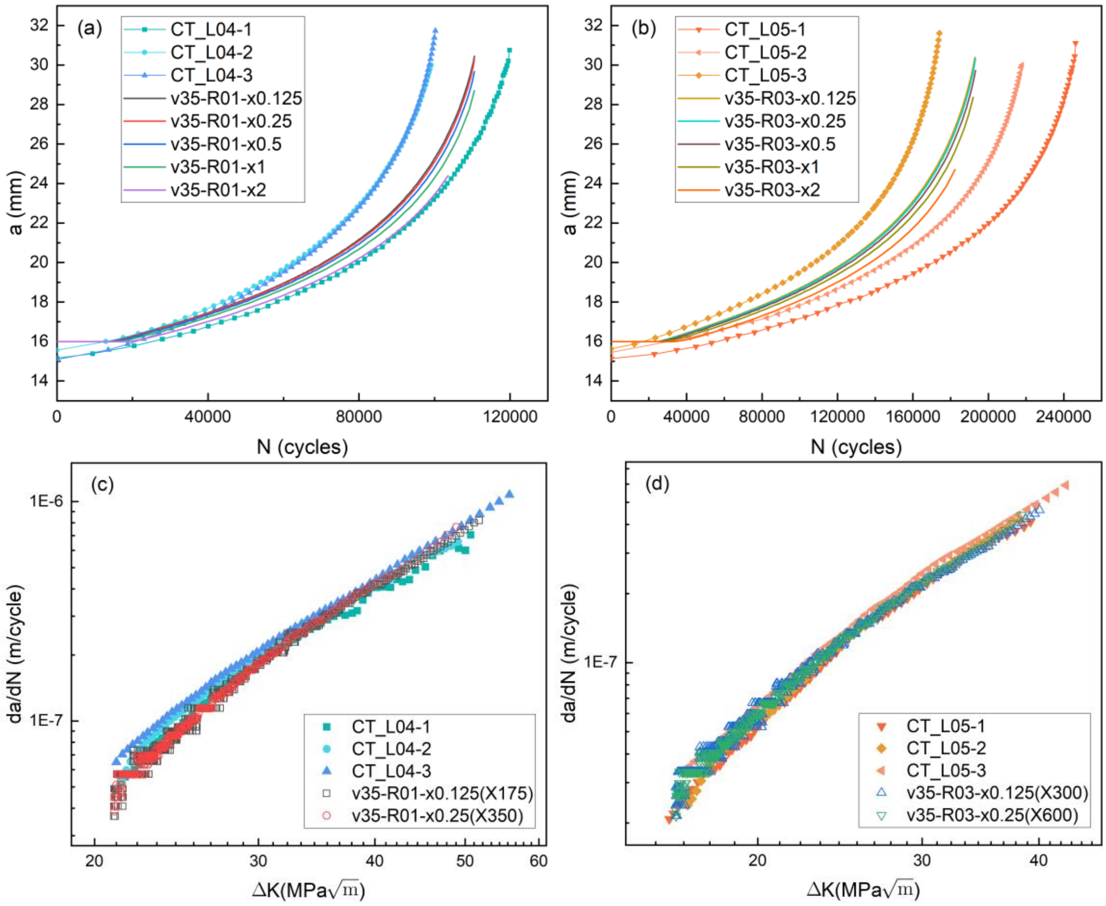

Fig. 8. Simulation results of CCZM v35. (a) $a - N$ curves at the load ratio of 0.1, (b) $a - N$ curves at the load ratio of 0.3, (c) rate curves at the load ratio of 0.1, and (d) rate curves at the load ratio of 0.3. (test data are extracted from Ref [41])

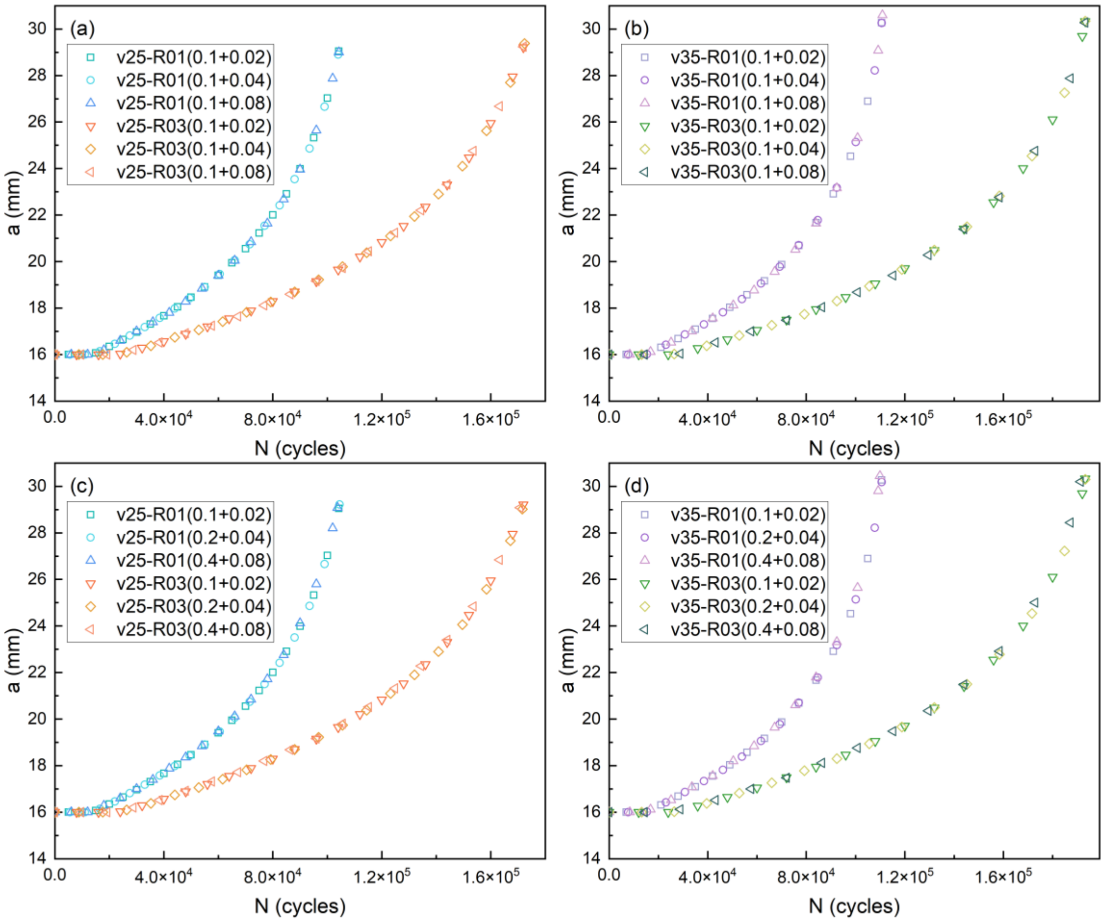

Fig. 9. Robustness study. (a) the effect of different cohesive element sizes with CCZM v25, (b) the effect of different cohesive element sizes with CCZM v35, (c) the effect of different matrix element sizes with CCZM v25, (d) the effect of different matrix element sizes with CCZM v35.

Table 1 Calculated values of fracture toughness

Specimen label	B (mm)	W (mm)	a_0 (mm)	F_Q (kN)	F_m (kN)	K_Q $(\mathrm{MPa}\sqrt{\mathrm{m}})$	$\delta_{m(12)}$ (mm)
DL1	12.15	48.12	24.26	15.40	23.84	56.66	0.207
DL2	12.10	48.27	24.27	14.64	23.70	53.91	0.192
DL3	12.09	48.25	24.39	15.81	24.04	58.69	0.244

Table 2 Parameters in the cohesive zone model for the simulation of fracture toughness tests.

$\sigma_{max,0}$ (MPa)	δ_0 (mm)	Stress state	Fracture toughness used for calculation
1290	0.00401	plane strain	mean K_Q
1075	0.00481	plane strain	mean K_Q
860	0.006015	plane strain	mean K_Q
1290	0.05153	plane strain	mean $\delta_{m(12)}$
1075	0.06183	plane strain	mean $\delta_{m(12)}$
860	0.07729	plane strain	mean $\delta_{m(12)}$
1290	0.00441	plane stress	mean K_Q
1075	0.00529	plane stress	mean K_Q
860	0.00661	plane stress	mean K_Q
1290	0.02061	plane stress	mean $\delta_{m(12)}$
1075	0.02473	plane stress	mean $\delta_{m(12)}$
860	0.03092	plane stress	mean $\delta_{m(12)}$

Table 3 Comparison between plane stress simulation results and test values.

$\sigma_{max,0}$ (MPa)	δ_0 (mm)	F_{max} + (percent error) (kN) + (-)	CMOD at F_{max} + (percent error) (mm) + (-)
1290	0.00441	24.47 (2.56%)	1.92 (21.52%)
1290	0.02061	25.90 (8.55%)	2.14 (35.44%)
1075	0.00529	23.34 (2.18%)	1.28 (18.99%)
1075	0.02473	25.20 (5.62%)	2.07 (31.01%)
860	0.00661	21.99 (7.84%)	0.96 (39.24%)
860	0.03092	24.12 (1.09%)	1.48 (6.33%)